Computational Modeling of Turbulent Flows on the Tip Vortex of a Marine Propeller's Blade

Liad Paskin, Michel Visonneau, Emmanuel Guilmineau, Jeroen Wackers

Computational Modeling of Turbulent Flows on the Tip Vortex of a Marine Propeller's Blade

Liad Paskin, Michel Visonneau, Emmanuel Guilmineau, Jeroen Wackers
LHEEA UMR-CNRS 6598, École Centrale Nantes, France

ABSTRACT

Present work evaluates the numerical modeling of tip vortex flows, with particular emphasis on the turbulence modeling required for cavitating conditions. The high Reynolds flow on a hydrodynamic NACA 66_2-415 profile is numerically addressed with the finite volume solver ISIS-CFD. The turbulence models explored are: $k-\omega$ SST; EARSM with curvature correction; and hybrid RANS-LES, DES-SST. An adaptive grid refinement (AGR) technique is employed to suggest an optimized spatial discretization procedure. The predictions of these turbulent models are compared for different flow quantities probed in the vortex core. Comparison to experimental data for the vertical velocities indicate the accuracy of the DES-SST model; while the statistical models are unable to capture multiple critical flow features, such as the magnitude of the pressure drop on the vortex core and the vortex intensity. The AGR methodology is confronted to a non-AGR case confirming its suitability and efficiency. Exploring the DES obtained vortices and anisotropic Reynolds stress tensor, some inherent URANS models' limitations are exemplified and discussed.

1 INTRODUCTION

An incident flow on a lifting profile creates the pressure difference that generates lift or thrust, caused by the flow circulation around the body. Circulation, lift, and pressure differences smoothly drop to zero at the wing tip, where loading is null. This three dimensional behavior generates a complex flow pattern where the circulation is redistributed into multiple vorticity structures, i.e., vortex sheets, lines or singularities (see Jiménez 2004), which generated in the boundary layer interact with each other while advected by the mean flow.

The vorticity generally observed on a three dimensional lifting profile may be grouped into two systems with particular behaviors. The first is the the body's wake, created close to the trailing ledge along the wing span. The second refers to the vortex created at the tip of the wing in an axisymmetric, structured swirling pattern. The tip vortex interacts and eventually consumes the body's wake in a process known as roll-up, feeding from its kinetic energy and vorticity until its circulation matches the one at the wing (Asnaghi 2018). Downstream, viscous forces eventually damp out the vortex structure that becomes unstable and finally dissipates. Other well defined vorticity systems appear where the wing joins another body, such as the horse shoe vortex tube on the leading edge and the base trailing wake at the trailing edge, of the joint region.

Interactions between the wake and the tip vortex are highly non-linear, being sensitive to local and fine flow characteristics that should be captured on any accurate modeling attempt. The tip vortex includes steep pressure and velocity gradients, and specific disturbances such as minimum pressure zones and fluctuations appear on the tip vortex core and its interaction with the wake vortex system. Moreover on engineering applications the flow is generally turbulent, and in marine applications cavitation is expected.

This work focus on the turbulence models' evaluation, so to provide an accurate description of the incompressible, single-phase, turbulent flow required by further cavitation analyses. Being marked by the complex flow here described as three dimensional, anisotropic non-linear motions, the turbulence observed on the tip vortex can be hardly modeled by the current usual CFD techniques (Pope 2000). Unlike molecular diffusion, turbulence occurs in time scales comparable to the mean flow: Being it submitted to rapidly changing shear stresses, it can be hardly described exclusively by local quantities such as the local shear stress tensor. It is likely that turbulence memory becomes important, and a sufficiently accurate description of turbulence history is then required to go beyond the eddy viscosity hypothesis. The DES-SST is capable of resolving turbulent scales beyond the average one, thus allowing the fine description of the mentioned phenomena.

One test case is considered and described in section 2, being the numerical strategy introduced in 3. Results and discussion come in section 4, followed by conclusion in 5.

2 TEST CASE

The present case (figure 1) focuses on the tip vortex dynamics and has been subject to different studies about tip vortex cavitation. The hydrodynamic elliptical Arndt foil adopts a NACA 66_2-415 profile (Arndt et al. 1991; Pennings 2016; Asnaghi 2018), which presents low adverse pressure gradient and delays boundary layer detachment. The trailing edge is truncated at a thickness of 0.3 mm due to manufacturing limitations. The numerical domain is designed to mimic the experimental facility reported by (Pennings 2016), from which results are here compared. The experimental reference employs a PIV technique for obtaining a fine description of the the velocity field around the tip vortex core at 5 different longitudinal sections x = {6.3; 9.3; 14.3; 22; 69} cm.

The blade has span $l = 15$ cm and base chord $c = 12.56$ cm. The origin is positioned so that the tip coordinates are $[0,0,l]$. The fluid domain extends from $[-4l < x < 10l, -l < y < l, 0 < z < 2l]$. The fluid properties are $\rho = 997$ kg/m^3 and $\mu = 9.5\text{e-}04$ kg m^{-1} s^{-1} so that with an inlet velocity $U = 6.8$ m/s, the Reynolds number is $Re = 8.96 \cdot 10^5$. A single angle of attack is considered: $AOA = 9^o$. The developed surface area is $S = 146.5$ cm^2.

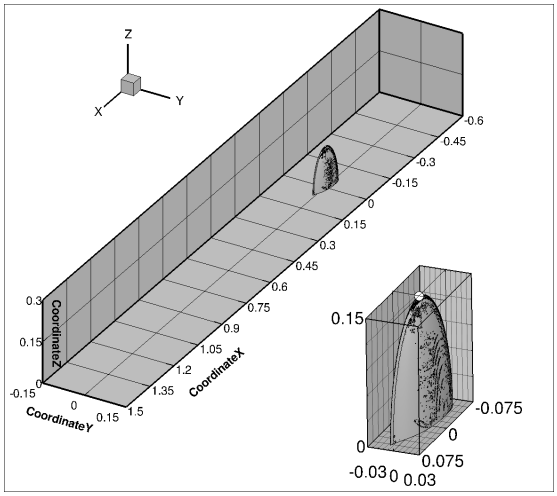

Figure 1: Geometry.

Free-Slip condition is imposed on upper ($z = 2l$) and lateral ($y = -l, l$) boundaries/ walls. No-slip condition is imposed on the elliptic body and on the floor at $z = 0$. The flow is prescribed at the inlet $x = -4l$ with uniform longitudinal velocity $\overline{u}_x = U$. Turbulent quantities on the inlet are: Turbulent kinetic energy $k = 5.167 \cdot 10^{-8}$ m^2/s^2, dissipation $\varepsilon = 2.522 \cdot 10^{-7}$ m^2/s^3, and frequency $\omega = 54.23$ Hz. The prescribed pressure on the outlet at $x = 10l$ is null.

3 NUMERICAL STRATEGY

The computational modeling of fluid dynamics (CFD) is here performed with the solver ISIS-CFD, developed by the METHRIC team of (LHEEA, CNRS/ECN) and distributed by NUMECA within the FINE(TM)/Marine package. The incompressible flow solver ISIS-CFD (Queutey and Visonneau 2007) is based on a face-centered finite volume discretization adapted to two or three-dimensional fully unstructured grids. The Unsteady Reynolds Averaged Navier Stokes equations are solved on a possibly moving grid for different turbulent closures. The momentum conservation equations are solved for the velocities while incompressibility constraint leads to a Poisson equation which is solved for the pressure. For turbulent flows, additional transport equations are solved according to the chosen turbulence closure. Spatial derivatives are evaluated with second order accuracy, usually discretized by a central approximation scheme. Upwinding may be imposed on the convective terms, e.g., by the GDS, or a specified blending of Central-Upwind schemes. For unsteady computations, time derivatives are evaluated with second order accuracy by a three-level Euler time marching scheme. Pressure-velocity coupling is achieved by a Rhie and Chow SIMPLE algorithm.

Two Unsteady Reynolds Average Navier Stokes equations (URANS) closures are considered: $k-\omega$ SST and EARSM models. The $k-\omega$ SST model (Menter 1994) is a two equation closure blending between $k-\omega$ and $k-\varepsilon$ models on the body's vicinity and far field respectively. The Explicit Algebraic Reynolds Stress model (EARSM) introduces several simplifications to the exact Reynolds Stress Tensor (RST) equations (Deng and Visonneau 1999), thus allowing an explicit approximated solution for the Reynolds Stresses Anisotropy, which is added to the $k-\omega$ SST solution such that the RST is determined not only by the local shear stresses but also by rotation. The EARSM model is here applied with a curvature correction which artificially reduces the modeled stresses inside the vortex (Deng and Visonneau 2003).

An implicit filter is applied to the Navier Stokes equations by a Detached Eddy Simulation (DES) approach, capable of performing a smooth transition between URANS and LES formulations according to the local grid sizes. Where the grid is too coarse to capture the energy containing scales of turbulence, DES solves URANS equations, for example, through the $k-\omega$ SST model (Strelets 2001). When the grid becomes fine enough for an LES, modeled diffusion is dissipated, implicitly implying the filter to the velocity field, thus allowing turbulence unsteadiness to be resolved into the larger, energy containing part of the turbulent energy spectra.

A careful description of the applied turbulence models can be, hopefully, better appreciated in (Paskin 2018). Current work applies the GDS scheme with a fixed time step $\Delta t = 1e-03$ s to URANS models, and a 5% upwind blended scheme for DES-SST where $\Delta t = 5e-05$ s.

3.1 Adaptive Grid Refinement

The small scales flow features in the tip vortex impose severe requirements on the grid size. An efficient grid is then desired to reduce the computational costs of the numerical experiments. The main difficulty in building a complex flow grid is to correctly capture the critical refinement zones which require lower grid size than the undisturbed free stream zone. Extending this local requirement to the whole domain leads quickly to unaffordable grid sizes but on the other hand one cannot precisely identify the critical zones a priori, i.e., without exploiting a reliable numerical solution. Adaptive grid refinement (AGR) is a numerical tool capable of identifying and refining the critical zones as the flow evolves in a given simulation.

The adaptive grid refinement available in ISIS-CFD refines unstructured hexahedral grids by consecutive division of the cells. Anisotropic grid refinement is employed and the mesh updated dynamically during the computation. Previously refined cells can be unsplit if the refinement is no longer required. The cells are redistributed among the partitions to avoid over refinement of a single processor. A detailed presentation and discussion about the AGR method applied is presented by (Wackers et al. 2017). Protective measures are available to ensure the mesh quality and the ones here applied are the minimum cell size and a minimum protection of the boundary layer.

The anisotropic refinement relies on a metric tensor field $\boldsymbol{C}_i$ as the criteria and the constant T_r as threshold. The cell sizes are evaluated for a cell i as the vector $\boldsymbol{d}_{i,j}$ joining the opposing face centers on the direction j. The cell i is refined on the direction j if $||\boldsymbol{C}_i\boldsymbol{d}_{i,j}|| > T_r$ and derefined if $||\boldsymbol{C}_i\boldsymbol{d}_{i,j}|| < T_r/f$ where on present computations $f = 2.5$. The criteria is based on the Hessian matrix of second spatial derivatives, which give an indication of the discretization error for second order schemes. Both pressure and velocity field Hessian matrices are taken into account by the flux-component Hessian criterion.

3.2 Grids

Two grids are considered, either employing or not the adaptive grid refinement technique. The main design constraint is that they possess at least 4 cells per estimated Taylor scale on the vortex core, at the 4 closest-to-body probing sections. Given the kolmogorov ($\eta \sim l_0 Re^{-3/4}$) and integral length ($l_0 \sim c$) scales, the Taylor scale is estimated (Pope 2000) as $\lambda \sim \sqrt{10}\eta^{2/3} l_0^{1/3} = 0.4mm$.

The original mesh built in Hexpress for the AGR methodology is composed of 6.461 M cells and guarantees $y+ < 1$ on the blade and $y+ \sim 30$ on the plate. The cell sizes on the boundaries are exposed in table 1.

Table 1: Cell sizes on the boundaries for the original Hexpress grid.

	1st cell perp. size	**1st cell paral. size**	**Nb of layers**	**Ratio**
Blade faces	2.5e-06 m	1.25 mm	42	1.15
Trailing edge	2.5e-06 m	0.625 mm	42	1.15
Tip	2.5e-06 m	0.3125 mm	42	1.15
Plate	5e-05 m	10 mm	10	1.20
Other	10 mm	10 mm	N/A	N/A

A global AGR refinement is first employed with the $k-w$ SST model resulting in 10.25 M cells when Tr = 0.035. Further refinement was limited to $-5\text{mm} < x < 45cm$, $-15\text{mm} < y < 15\ mm$, and $11\text{ cm} < z < 15.5cm$. The refinement threshold was lowered to 0.0125, and the nominal minimum size to 0.125 mm so that the actual minimum size is around 0.0781 mm. Between each computation the grid is frozen so that derefinement cannot coarsen a previously converged mesh. The process combines $k-w$ SST and EARSM computations to extend the refined zones. The resultant mesh has 51.97 M cells.

The AGR method is not available for the DES turbulence model in ISIS-CFD, so that the AGR grid matches URANS predicted local flow features, that differ from the DES resolved computations. A comparison between AGR and manually adapted grids is then desired, being here carried with respect to a Hexpress, non-AGR grid of 64.26 M cells.

The non-AGR grid is built with different refinement zones superposed to the initial 6,461 M cells grid. Four boxes are defined with characteristics exposed in table 2 so that $xi < x < xf$, $yi < y < yf$, and $zi < z < zf$. Two concentric, cylindrical refinement zones of circular sections track the vortex trajectory previously obtained with $k-\omega$ SST computations. The outer section has variable radius $10\text{ mm} < r_1 < 20\text{ mm}$, enlarging stream-wise of the blade, and imposes anisotropic cell sizes of {0.312,0.156,0.156} *mm* on {x,y,z} directions. The inner section has constant radius $r_2 = 5$ mm and imposes cell sizes of {0.156,0.078,0.078} *mm*.

Table 2: Refinement boxes. Cell sizes and bounds in *mm*.

ID	**Size**	*xi*	*xf*	*yi*	*yf*	*zi*	*zf*
01	5.00	-225	750	-30.0	30.0	0	175.0
02	2.50	-175	500	-20.0	20.0	0	160.0
03	1.25	-125	450	-17.5	17.5	0	155.0
04	0.62	0	250.0	-22.5	12.5	0	152.5

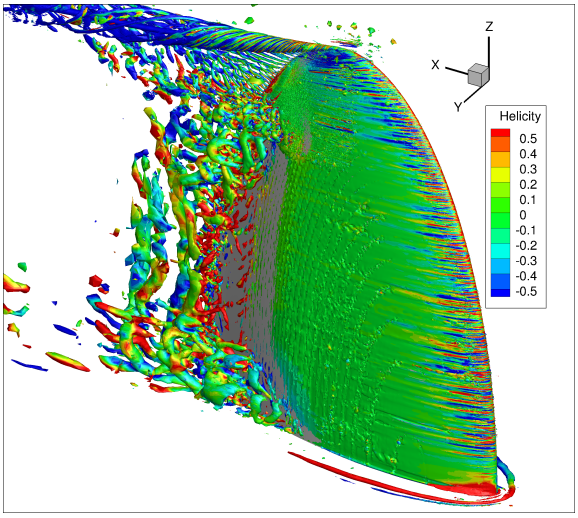

(a) AGR grid; 52 M cells.

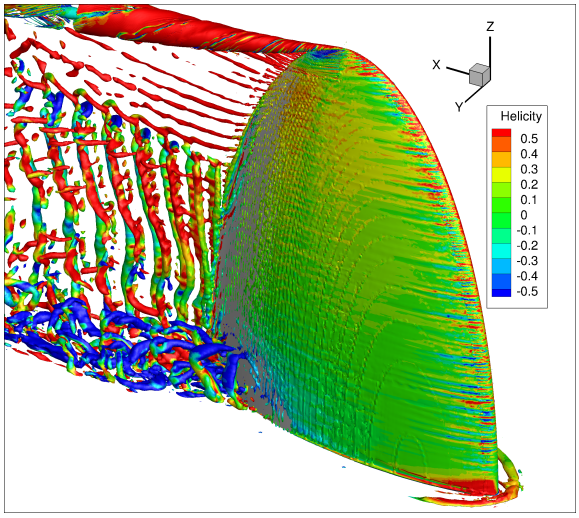

(b) Non-AGR grid; 64 M cells.

Figure 2: Instantaneous field for DES-SST: Iso-surfaces $Q^* = 50$ colored by normalized helicity.

4 RESULTS

4.1 Visualization

The normalized second invariant of the velocity gradient $Q^* = Q/(U/L)^2$ identify the vortex structures by a specified threshold $Q^* > 50$, so that the iso-surfaces $Q^* = 50$ of figure 2 reveal the resolved instantaneous vortices, colored by the normalized helicity, which measures the alignment between the helical structures with respect to the local stream-wise direction. When vorticity structures of opposite helicity sign meet, the counter rotating vortices merge as the least energetic ones are consumed by, and supply their momentum to, the strongest; If the helicity of the meeting vortices has equal sign, they rotate on the same direction and the interaction leads to vortex break-down and instabilities with the collision of streamlines of opposite senses.

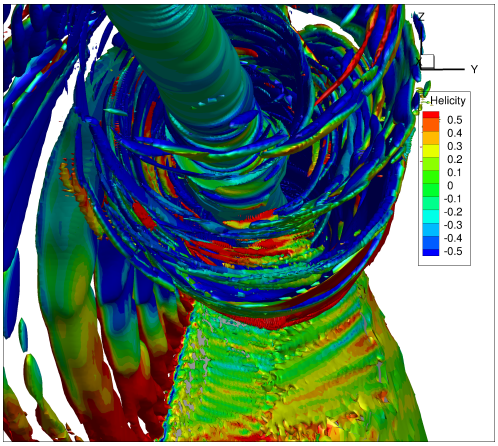

Figure 3: Instantaneous field for non-AGR DES-SST.

The horse-shoe vortex is captured on the juncture between the leading edge and the plate in figure 2. Multiple stream-wise vortices rise on the leading edge with opposite rotation, merge into a perpendicular direction (not captured, but modeled hairpin-like turbulent structures) and are convected through the body to the tip vortex or the wake. The modeled turbulence is suppressed as the flow leaves the body so one appreciates the large scale turbulent vortices that leave the trailing edge merging into the tip vortex. The tip vortex emerge from the vorticity recently generated on the on the leading edge.

Most of the vorticity generated along the body departs from the trail edge and merges into the tip vortex along the roll up. The interaction occurs in a variety of scales, whose complexity is indicated by figure 3. The breakdown occurs as the structured patterns approach the tip vortex, being submitted to increased strain and turbulence, and split into smaller structures. Eventually no structured pattern is observed: The vortices have been assimilated at such small turbulent scales, they cannot be discerned by the filter or criteria.

Being the AGR grid (figure 2a) based on statistical first order closure models, comparison is presented to a manually adapted grid (figure 2b), to address whether the observed structures are grid induced. A remarkable feature found in both computations are the smaller stream-wise vortices that depart from the trail edge, where the grid is fine enough, i.e., closer to the tip vortex. The implicit filter imposed by the Hybrid DES-SST model implies that in different regions of grid refinement, the structures observed with the defined criteria occur in different scales. The non-AGR grid captures an alternate vortex detachment

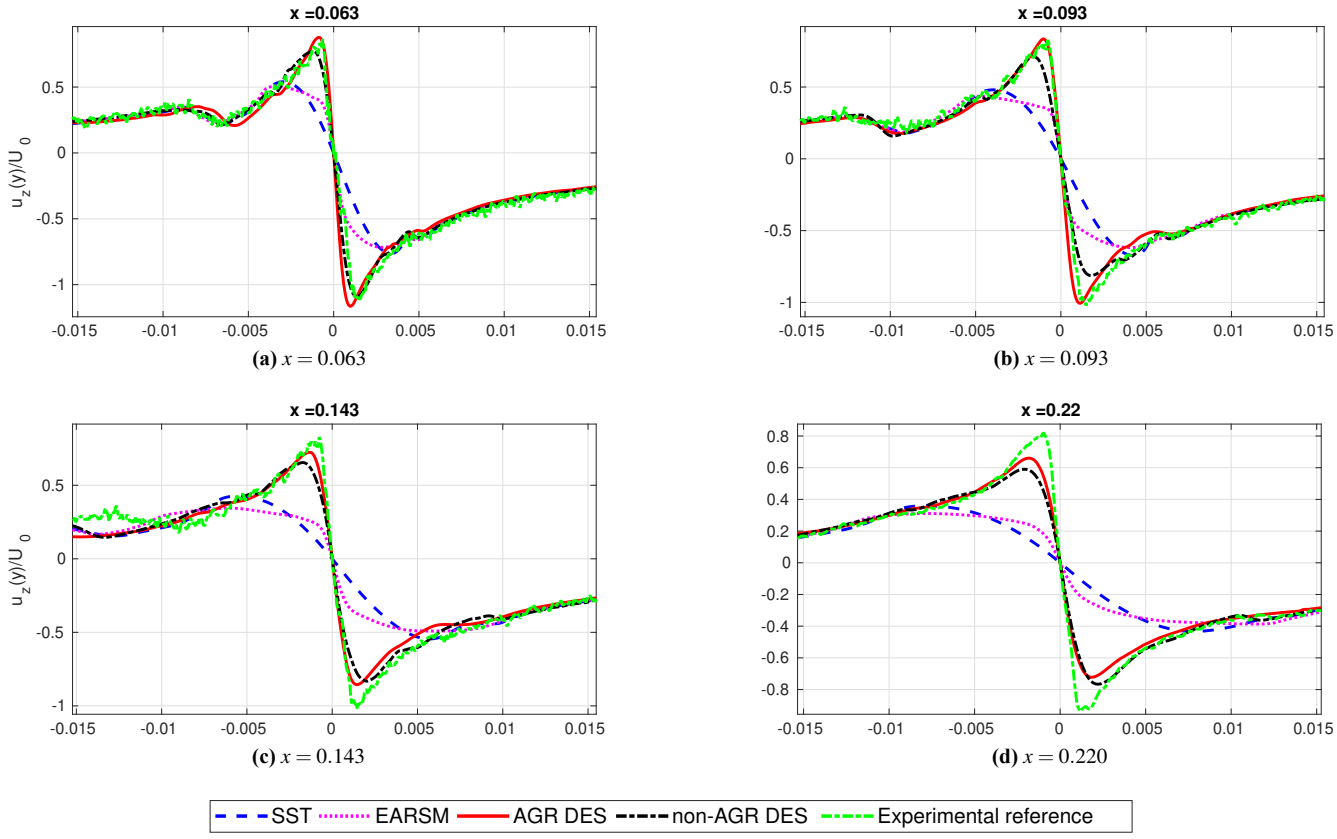

(a) $x = 0.063$ **(b)** $x = 0.093$ **(c)** $x = 0.143$ **(d)** $x = 0.220$

Figure 4: Normalized $u_z(y)$ profiles through the vortex core at $z = z_c$

pattern on the wake, while the AGR grid captures the fully turbulent, large structures on this region. Most likely, all those structures coexist though the observable pattern depends on the filter and the criteria. Long averaging periods would lead to the predominance of vortex sheet structures such as obtained with URANS formulations (figure 5).

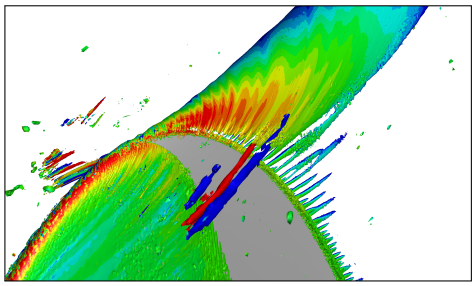

Figure 5: Instantaneous field for $k-\omega$ SST.

4.2 Vortex core profiles

Flow properties are evaluated along the vortex core and through five probing sections defined according to the available experiments. The PIV experiments provided by (Pennings 2016) include a fine description of the velocity fields on these sections, which is compared with the present numerical results. The profiles of figures 4, 7 and 9 refer to horizontal probes, within a local frame of reference centered at the core, and show the vertical velocity u_z, pressure p and turbulent kinetic energy k respectively. Other quantities are explored in (Paskin 2018).

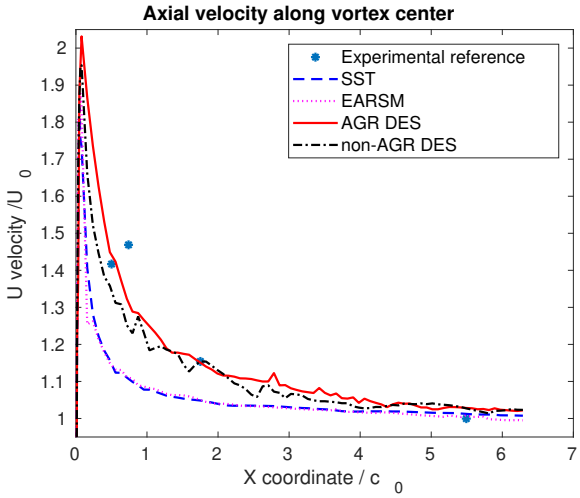

Figure 6: $u_{x,max}(x)/U_0$ profiles through the vortex core

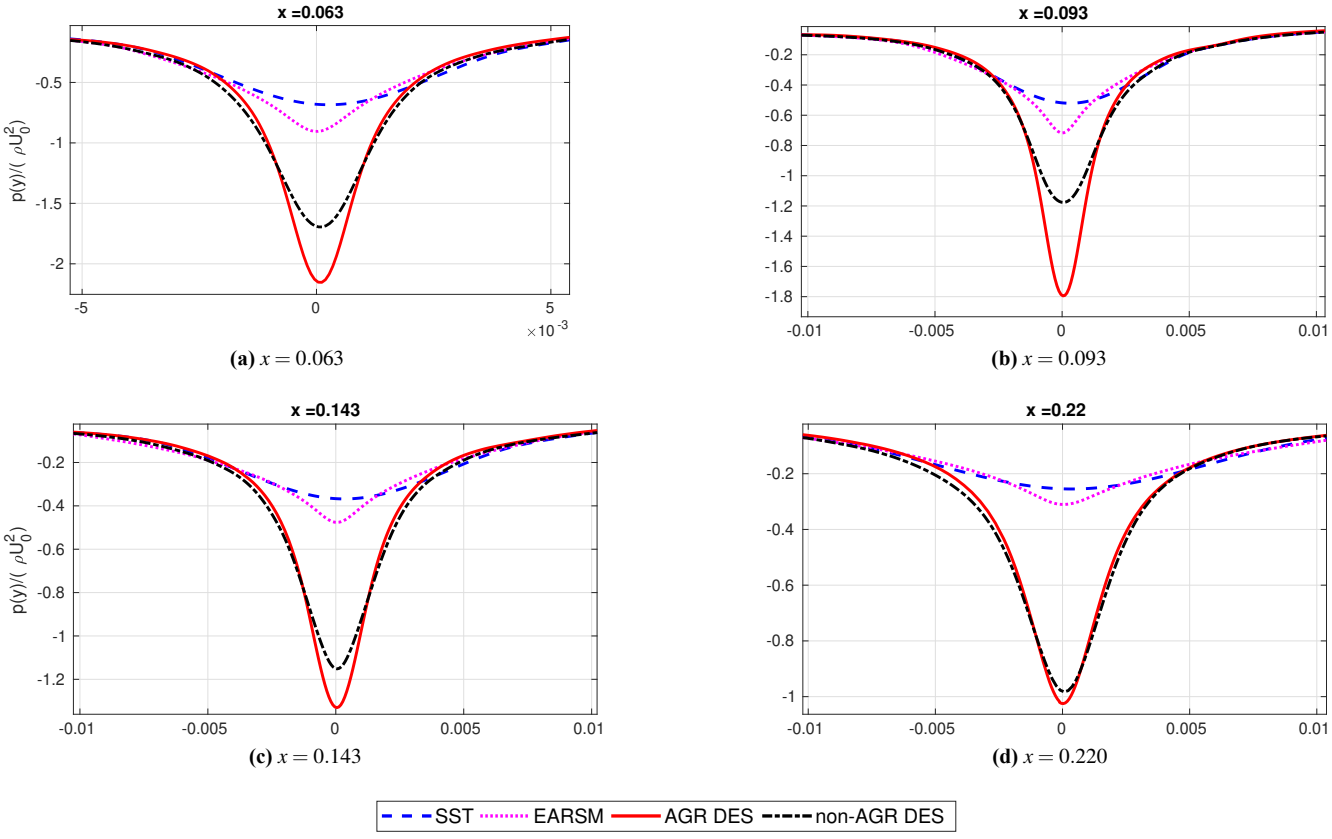

(a) $x = 0.063$ **(b)** $x = 0.093$ **(c)** $x = 0.143$ **(d)** $x = 0.220$

Figure 7: Normalized $p(y)$ profiles through the vortex core at $z = z_c$

The AGR grid (52 M cells), DES vertical velocity profiles corresponds well to the experiments on figures 4 and 6. The resemblance is degraded downstream, where the grid coarsening begins to affect the flow dynamics. Comparing the DES results to the alternative URANS techniques, it appears that resolving the unsteady turbulent dynamics is imperative to capture the vortex local behavior, and particularly features such as the vortex size and velocity extremes.

The implicit filter of the hybrid DES-SST method implies that the discretization determines the modeling error. Disposing of a higher number of cells (64 M), the non-AGR grid results present increased modeling error compared to the AGR case (52 M). The adaptive grid refinement is thus found to be a powerful tool for minimizing the modeling error in DES computations.

The mean pressure profiles are shown in figures 7 and 8, and suggest that the URANS models are incapable to capture the correct pressure field, and thus unsuitable to model cavitation dynamics.

The EARSM-CC model does provide a slight improvement with respect to the $k-\omega$ in capturing the steep gradients at the center of the velocity profiles (figure 4) or the minimum pressures (figure 7), but still reveals the modeling errors inherent to first order statistical models.

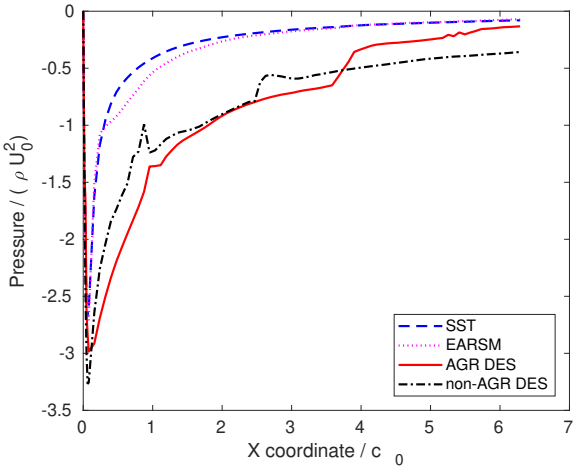

Figure 8: $p_{x,min}(x)/(\rho U_0^2)$ profiles through the vortex core

The total turbulent kinetic energy k is decomposed into modeled and resolved parts (figure 9). By artificially suppressing the modeled turbulent kinetic energy on the

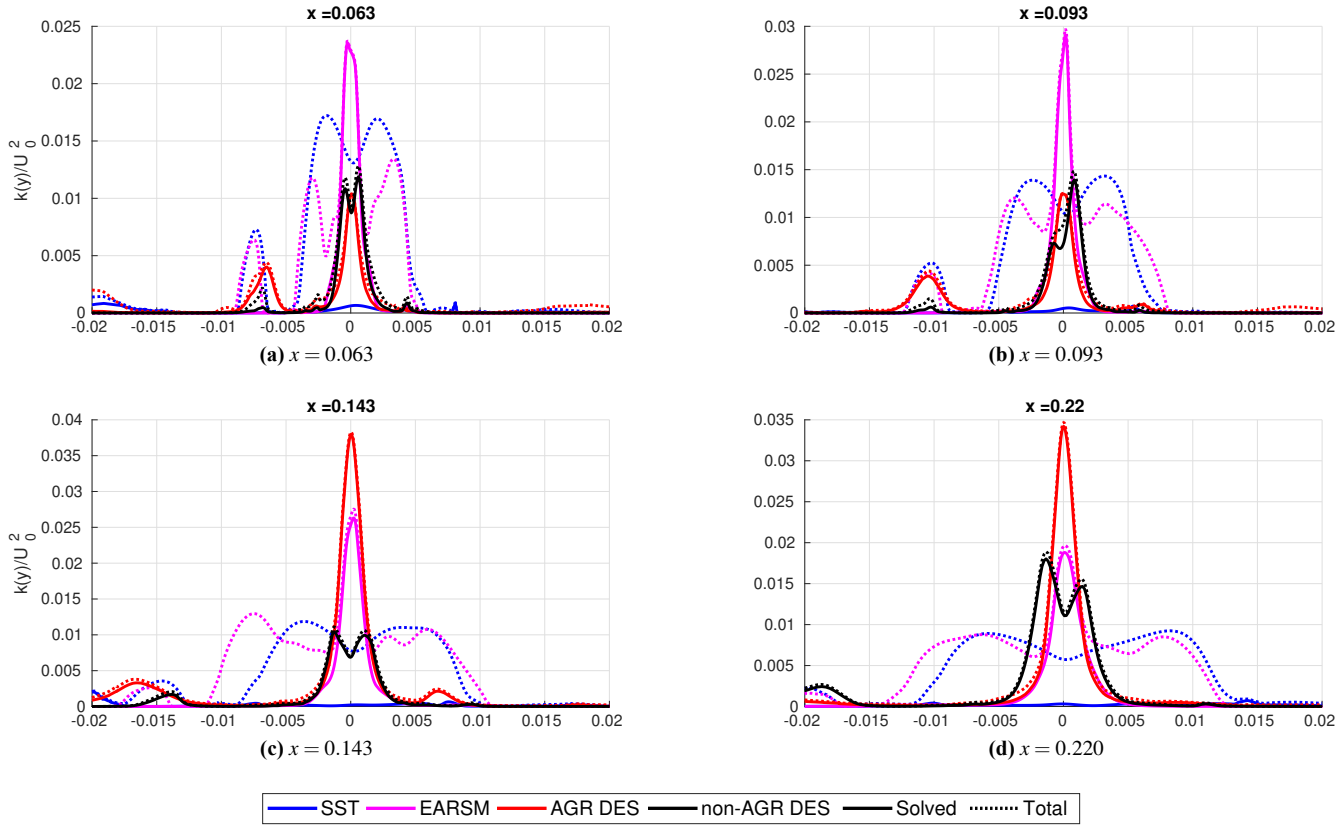

Figure 9: $k(y)/(U^2)$ profiles through the vortex core at $z = z_c$

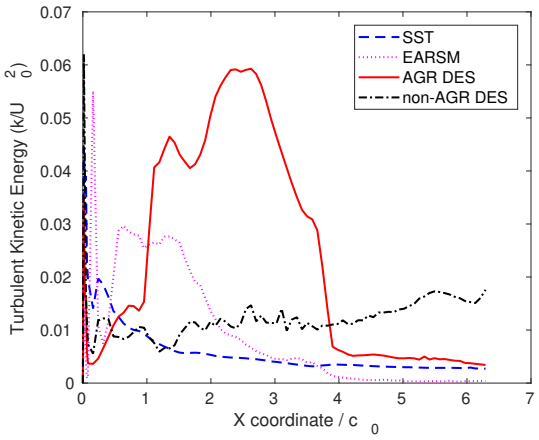

Figure 10: $k_{x,c}(x)/(U^2)$ profiles through the vortex core

vortex core, the curvature correction applied with EARSM model, locally allows the development of the velocity field fluctuations in a similar way as DES-SST. However, for DES-SST the modeled k is suppressed through the whole profile leading to significantly different total distributions. Curiously, by suppressing the modeled turbulent kinetic energy, the EARSM induces higher values of total k in the vortex center. Though the non-AGR grid has much of its turbulent momentum resolved, a small amount of modeled k is observed by subtracting solved from total k profiles in figure 9. Generally, a maximum value of k is obtained in the core when resolved turbulent motions are considered. The stronger the vortex, lesser its span, longer its extend, and closer the k profiles from having a single-peak shape at the vortex core.

Considering the vortex emerges on the tip, while most of the turbulence is created through the boundary layer, the importance of the roll up becomes evident in evaluating the evolution of k along the vortex core at figure 10: It is the mechanism by which most of the body-generated turbulence is finally assimilated by the tip vortex.

4.3 Reynolds stress tensor anisotropy

The Reynolds stress tensor $\boldsymbol{\tau}^{(r)} = -\rho\overline{u_i' u_j'}$ imposes the coupling between the mean and fluctuation fields, resuming the turbulence influence on the mean flow so that its description by mean flow quantities is the primary objective of URANS methodologies. The turbulent eddy viscosity hypothesis common to the applied statistical models states that $\boldsymbol{A}$, the anisotropic part of $\boldsymbol{\tau}^{(r)}$, is defined by the local mean shear stress tensor $\boldsymbol{S}$, weighted by a scalar turbulent viscosity analogous to molecular diffusion. The hypothesis

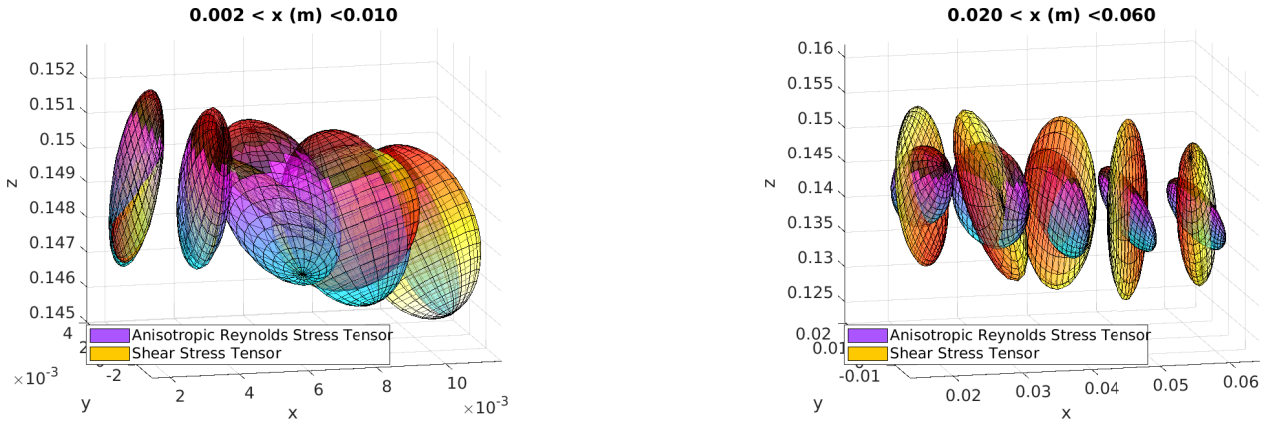

Figure 11: Lamé ellipsoids for the Anisotropic Reynolds Stress and the Shear Stress Tensors.

often fails, being the $\boldsymbol{A}$ not aligned with $\boldsymbol{S}$, and dependent on other phenomena such as rotation and history (Pope 2000).

The DES methodology allows the resolution of most of $\boldsymbol{\tau}^{(r)}$. A graphical representation of a tensor $\boldsymbol{\tau}$, known as the Lamé ellipsoid, is obtained by rendering a surface on the end points of all vectors $T_\alpha = \boldsymbol{\tau} \cdot n_\alpha$ starting at the origin, expressing the projection of $\boldsymbol{\tau}$ on all directions simultaneously. The obtained surface is an ellipsoid, oriented into the eigenvectors and with semi-axis corresponding to the eigenvalues of the tensor.

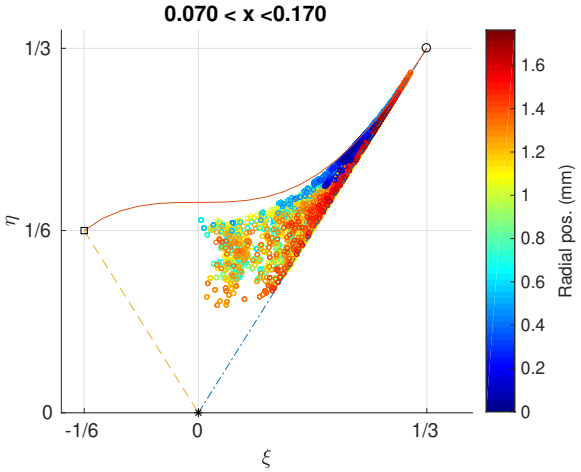

Figure 12: Lumley triangle and the Reynolds Stress Anisotropy at the core.

The validity of the eddy viscosity hypothesis is evaluated in figure 11, superposing the Lamé ellipsoids for $\boldsymbol{A}$ and $\boldsymbol{S}$ obtained in the vortex center with AGR DES-SST, centered at the probing position. The tensors are normalized per probe, being the discussion limited to the stresses shape, not its magnitude. Close to the body, URANS takes place, and the Reynolds Stress Anisotropy agrees to the eddy viscosity hypothesis, presenting an axisymmetric, one lower component turbulent state. As the modeled turbulence is suppressed, $\boldsymbol{A}$ assumes the cigar structured configuration, rapidly deviating from a scalar relationship to $\boldsymbol{S}$. The principal directions and eigenvalues ratios strongly differ from what is predicted by the Eddy Viscosity hypothesis. Nevertheless, both structures are still correlated on a cigar shape.

An invariant 2D map (see Lumley triangle on Pope 2000) which fully describes $\boldsymbol{A}$ is exploited in figure 12; its colors revealing the correlation between the anisotropic state and the radial positions. Probing takes place in $Q^* < 50$, where the Reynolds Stress Tensor obtained in the center is gathered close to a one-component turbulence state, while the rest of the vortex is gradually distributed from the two-components to the axisymmetric (one high value) state.

5 CONCLUSION

Through the resolution of large turbulent motions by DES-SST, it have been discussed important flow features in tip vortex flows, otherwise not accessible with current URANS techniques such as the $k-\omega$-SST and EARSM here applied. The large scale turbulent vortices' renders allows a fine description of the flow physics. Velocity profiles on the core for DES-SST agrees well to the experiments, which is not true for URANS. Pressure profiles on the core suggests present URANS technique are unsuitable for cavitation analysis. The discussions about turbulent kinetic energy and Reynolds stresses anisotropy indicate inherent limitations of URANS techniques compared to DES-SST.

Further works can rely on the AGR methodology to perform a grid sensitivity analysis with respect to the refinement extent into the wake region, so to evaluate the present results and other fine resolution studies, e.g., spectral and turbulent kinetic energy budget analyses.

ACKNOWLEDGEMENT

This work was granted access to the HPC ressources of CINES under the location A0042A00125 made by GENCI (Grand Equipement National de Calcul Intensif).

REFERENCES

R. Arndt, V. Arakeri, and H. Higuchi. Some observations of tip-vortex cavitation. *Journal of fluid mechanics*, 229:269–289, 1991.

A. Asnaghi. *Computational Modelling for Cavitation and Tip Vortex Flows*. PhD thesis, 2018.

G. Deng and M. Visonneau. Comparison of explicit algebraic stress models and second-order turbulence closures for steady flow around ships. In *7th Symposium on Numerical Ship Hydrodynamics*, volume 10, page 5953, 1999.

G. Deng and M. Visonneau. On the prediction of swirling induced recirculation. In *TSFP DIGITAL LIBRARY ONLINE*. Begel House Inc., 2003.

J. Jiménez. Turbulence and vortex dynamics. Available at https://torroja.dmt.upm.es/area_alumnos/Introduccion_a_la_turbulencia/apuntes.pdf (26/04/2018), 2004.

F. Menter. Two-equation eddy-viscosity turbulence models for engineering applications. *AIAA Journal, vol. 32*, (8):1598–1605, 1994.

L. Paskin. A numerical assessment of turbulence modeling in tip vortex flows at cavitating conditions. Master's thesis, École Centrale de Nantes, 2018.

P. Pennings. *Dynamics Of Vortex Cavitation*. PhD thesis, TU Delft, 2016.

S. B. Pope. *Turbulent Flows*. Cambridge University Press, 2000.

P. Queutey and M. Visonneau. An interface capturing method for free-surface hydrodynamic flows. *Computers & Fluids*, 36: 1481–1510, 11 2007.

M. Strelets. Detached eddy simulation of massively separated flows. *AIAA Paper 2001-0879*, 2001.

J. Wackers, G. Deng, E. Guilmineau, A. Leroyer, P. Queutey, M. Visonneau, A. Palmieri, and A. Liverani. Can adaptive grid refinement produce grid-independent solutions for incompressible flows? *Journal of Computational Physics*, 2017.